Rotordynamic Computation of a Permanent-Magnetic excited Synchronous Machine due to Electromagnetic Force Excitation

M. Clappier, L. Gaul

For the acoustical computation of electromagnetic noise, it is very important to consider both, the rotor and stator vibrations of the electrical machine. Rotor vibrations can be transmitted as structure-borne sound to connected systems which might be excited at their resonances and radiate airborne sound. In order to predict the dynamical behaviour of complex electrical machine rotors (such like rotors of permanent-magnetic excited synchronous machines) in frequency domain, finite element (FE) computations can be efficiently applied using rotating coordinates. Hereby, it has to be taken into account that rotor vibrations are mainly influenced by stiffness and damping of the built-in laminated stacks and mechanical joints. Therefore, a FE model of the rotor is required which takes these parameters into account. In order to obtain the material properties, two experimental set-ups are considered. On the one hand, a generic lap joint is considered to determine the stiffness and damping of mechanical joints. On the other hand, a test rig for laminated stacks is presented which allows for the determination of direction-dependent stiffness and damping of laminated stacks by a shear and dilatation test. All identified parameters are included into the FE model. Thereby, local stiffness and damping of mechanical joints are modelled by so-called thin-layer elements. In order to prove the quality of the rotor FE model, a numerical modal analysis without considering rotor spin speed is carried out and compared to experimental results. Electromagnetic force densities are computed in the air gap of the electrical machine using an electromagnetic FE model. To cover different FE meshes of the mechanical and electromagnetic model, a method is presented which allows for converting force densities into equivalent nodal forces on the rotor surface. These excitation forces are used to compute electromagnetically caused rotor vibrations dependent on rotor spin speed by a frequency domain rotor dynamic analysis.

1   Introduction and Aim of this Work

Acoustical noise of electrical machines is made up of three different types of sources: electromagnetically, mechanically and aerodynamically excited vibrations/noise (Gieras et al., 2006). Electromagnetically caused vibrations result from electromagnetic forces in the air gap between rotor and stator (Gieras et al., 2006). These forces are mainly affected by the magnetic design and operational conditions of the electrical machine. Mechanically caused vibrations are e.g. due to rotor dynamic loads, bearing defects or tolerances and shaft misalignments (Gieras et al., 2006). Aerodynamic noise normally occurs due to the noise of cooling fans (Gieras et al., 2006). For totally enclosed and water-cooled machine housings, the last type of source does not occur. For acoustical computations both, vibrations of the stator housing as well as rotor vibrations must be taken into account in order to model all structure-borne and airborne sound paths. Especially rotor vibrations can be transmitted to connected systems where airborne sound can be radiated additional to the sound radiated by the electrical machine housing.

The acoustical behavior of electrical machines has already been considered in many publications. Most of them are only related to vibrations and sound radiation of the machine housing caused by electromagnetic force excitation on stator teeth (with/without eccentricity effects), cf. (Dupont et al., 2014) and (Shiohata et al., 2011). Only in few works the rotor is included as additional component into the structural finite element (FE) model (see Humbert et al. (2012), McCloskey et al. (2014) and Pellerey et al. (2012)) and magnetic forces are applied on the rotor (see McCloskey et al. (2014) and Pellerey et al. (2012)).

So far, no publication has been found by the authors which considers the numerical computation of rotor dynamics due to distributed electromagnetic forces on the laminated stack (obtained from magnetic FE analysis) using structural three-dimensional (3D) solid FEs. Available works are based on either analytical rotordynamic models with one or a few degrees of freedom or FE models built up by beam elements, cf. (Arkkio et al., 2010), (Pellerey et al., 2012) and named references in (Pellerey et al., 2012). Therefore, this work is concentrated on 3D FE rotordynamic analysis in order to examine electromagnetically caused rotor vibrations.

As application case, the rotor of a permanent-magnetic excited synchronous machine (PMSM) is considered which consists of many single electrical sheets stacked together and positioned between two balancing discs onto the rotor shaft, see Figure 1. Thereby, the laminated rotor stack is pre-tensioned by both balancing discs.
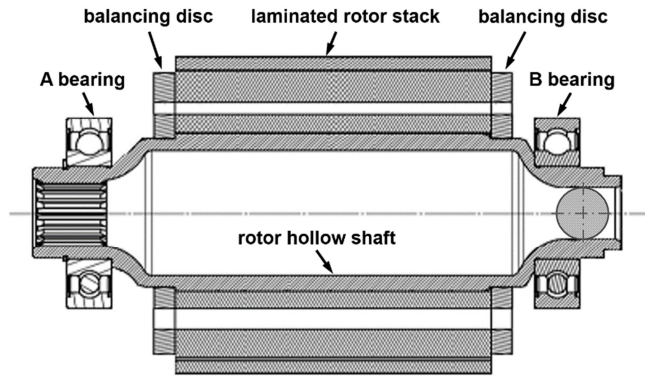
Figure 1. Rotor cross section of the considered PMSM rotor, cf. (Clappier and Gaul, 2016)

In order to carry out rotordynamic computations, it is very important to know the direction-dependent stiffness and structural damping of the laminated stack because both parameters mainly influence the dynamical behavior of the rotor. Normally, both quantities are unknown and estimated numerically via model updating, cf. (Gieras et al., 2006) for stators. The axial stiffness can also be determined load-dependent by a static compression test (Siegl, 1981). A detailed overview about literature and available approaches is given in (Clappier and Gaul, 2015). However, none of the named methods allows for the determination of structural damping and direction-dependent stiffness using only one experimental set-up.

In this paper, an experimental set-up is presented which allows for the determination of the direction-dependent stiffness and structural damping of laminated rotor stacks for certain pre-stress conditions using a shear and dilatation test. Based on these parameters, a FE model of the rotor is created. Thereby, so-called thin-layer elements (TLEs) are used to take the dynamics of several mechanical interfaces into account, cf. (Desai et al., 1984), (Gaul et al., 2011) and (Gaul and Schmidt, 2014). The computed eigenfrequencies, mode shapes and modal damping factors of the rotor (without spin speed) are compared to results of an experimental modal analysis (EMA). Finally, rotordynamic analyses are carried out to compute the response due to electromagnetic force excitation with and without taking dynamical rotor eccentricity into account. Thereby, a new method is presented to transform airgap forces from a two-dimensional (2D) electromagnetic computation onto a 3D structural mechanic FE mesh.

2 Experimental Determination of the Properties of Mechanical Joints and Laminated Rotor Stacks

2.1 Stiffness and Structural Damping of Mechanical Joints

Figure 2(a) depicts the experimental set-up of the considered generic lap joint (Gaul et al., 2015). Thereby, two masses m_1 and m_2 are supported by two thin wires at their center of gravity (Bograd et al., 2008).
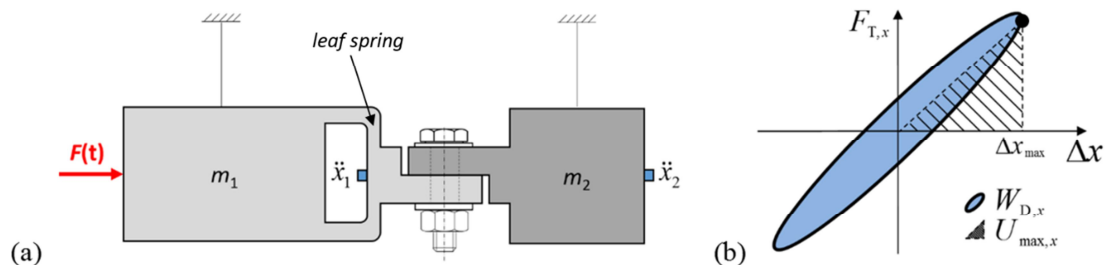
Figure 2. (a) Generic lap joint and (b) damping hysteresis, cf. (Bograd et al., 2008), (Gaul et al., 2016), (Gaul et al., 2011), (Gaul et al., 2015) and (Gaul et al., 1997)

Both masses are connected by a screw connection on a lap joint in order to define a certain interface contact pressure. Mass m_1 is excited harmonically with a certain excitation frequency and amplitude by an

electromagnetic shaker, cf. (Bograd et al., 2008) and (Gaul et al., 2015). Because of the leaf spring attached to mass m_1, a longitudinal system resonance is excited allowing to evaluate the structural damping of the mechanical joint up to high tangential forces (Bograd et al., 2008), (Gaul et al., 2015). When the set-up is in steady-state, the accelerations $\ddot{x}_1$ and $\ddot{x}_2$ of both masses are measured by two accelerometers (Bograd et al., 2008), (Gaul et al., 2015). Twice integration of both acceleration signals with respect to the time leads to the displacement signals x_1 and x_2, from which the relative displacement $\Delta x = x_1 - x_2$ can be computed (Bograd et al., 2008). Plotting the transmitted tangential force $F_{T,x} = m_2 \cdot \ddot{x}_2$ in the mechanical interface representing the inertia force of mass m_2 versus the relative displacement Δx leads to a hysteresis (Figure 2(b)), from which the tangential joint stiffness k_T and structural damping loss factor η can be derived by equations given in (1), see (Bograd et al., 2008), (Gaul et al., 2011) and (Gaul et al., 2015). Thereby, $W_{D,x}$ and $U_{max,x}$ are the dissipated damping energy and the maximum stored potential energy ((Bograd et al., 2008), (Gaul et al., 2011) and (Gaul et al., 2015)).

$$k_T = \frac{F_{T,x}(\Delta x_{max})}{\Delta x_{max}} \quad , \quad \eta = \frac{W_{D,x}}{2\pi \cdot U_{max,x}} \tag{1}$$

As it is shown in (Clappier et al., 2015b) and (Gaul et al., 2015), the joint damping loss factor strongly depends on the relative displacement, tangential force $F_{T,x}$ and normal force. Thus, this load dependency must be taken into account in FE models for applications with inhomogeneous contact pressure distributions, cf. (Clappier et al., 2015b) and (Gaul et al., 2016).

2.2 Stiffness and Structural Damping of Laminated Rotor Stacks

In (Clappier and Gaul, 2015), (Clappier et al., 2015a) and (Clappier and Gaul, 2016), a measurement set-up is presented for the determination of the direction-dependent stiffness and structural damping of arbitrarily shaped laminated structures. The experimental idea goes back to Crandall et al. (1971). The measurement concept is transferred and enhanced for measurements on laminated rotor stacks. A brief description of the measurement principle is given in the following according to Figure 3.
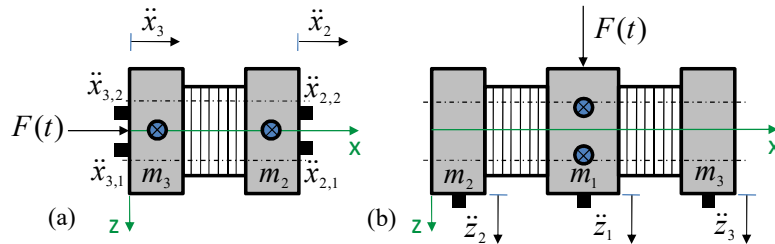
Figure 3. Measurement set-up for laminated rotor stacks. (a) Dilatation test and (b) shear test (Clappier et al., 2015a)

In order to determine the axial stiffness and structural damping of a laminated rotor stack, a dilatation test is applied (see Figure 3(a)) whereas a shear test is used for the determination of shear stiffness and structural damping (Figure 3(b)). Thereby, the measurement and evaluation idea is quite similar. In both configurations, one test specimen is axially pre-tensioned between two adjacent steel plates by screw connections (chain lines in Figure 3(a,b)). Thus, certain rotor prestress conditions can be considered. The masses of the steel plates (including the mass of the test specimen in distributed form) are denoted according to Figure 3(a,b) by m_1, m_2 and m_3. Both set-ups are supported at the metal plates by two thin wires as indicated by the crossed circular symbols. In order to examine the dissipative effects of the laminated stack, both set-ups are excited harmonically by an electromagnetic shaker. Thereby, the excitation direction differs by 90°. When the set-ups are in steady-state, the excitation force and acceleration of each metal plate are measured by a force sensor and accelerometers. Then, the relative displacement $\Delta x = x_3 - x_2$ (dilatation test) and $\Delta z_i = z_1 - z_i$ with $i = 2, 3$ (shear test) can be calculated by integrating the acceleration signals twice with respect to the time and subtracting them from each other. Plotting the transmitted normal force $F_{T,x} = m_2 \cdot \ddot{x}_2$ (index "T" denotes "transmitted") versus the relative displacement Δx (dilatation test) or $F_{T,z,i} = m_i \cdot \ddot{z}_i$ versus Δz_i with $i = 2, 3$ (shear test) leads to a hysteresis curve, cf. (Gaul and Schmidt, 2014) and Figure 2(b). Based on this hysteresis, the structural damping loss factors η_x (dilatation test) and $\eta_{z,i}$ (shear test) can be computed using the equations given in (2). Thereby, the dissipative damping energy $W_{D,x}$ or $W_{D,z,i}$ (from the dilatation or shear test) is divided by 2π times the corresponding maximum stored potential energy $U_{max,x}$ or $U_{max,z,i}$, cf. (Bograd et al., 2008) and (Gaul and Schmidt, 2014).

$$\eta_x = \frac{W_{D,x}}{2\pi \cdot U_{\max,x}} \qquad , \qquad \eta_{z,i} = \frac{W_{D,z,i}}{2\pi \cdot U_{\max,z,i}} \qquad , \qquad i = 2, 3 \tag{2}$$

The normal stiffness of the laminated stack for a certain pre-load F_N can be derived by the slope of the hysteresis, cf. (Gaul and Schmidt, 2014). The Young's modulus E can be computed using the normal stiffness k_x, initial thickness h_0 and cross section A of the test specimen. The shear modulus G is attained analogously using the shear stiffness $k_{z,i}$ (Gaul and Schmidt, 2014), see equations in (3). Further details can be found in (Clappier and Gaul, 2015) and (Clappier et al., 2015a).

$$E(F_N) = \frac{k_x(F_N) \cdot h_0}{A} \qquad , \qquad G_i(F_N) = \frac{k_{z,i}(F_N) \cdot h_0}{A} \qquad , \qquad i = 2, 3 \tag{3}$$

3   Finite Element Computation of electromagnetically caused Rotor Vibrations

3.1   Mechanical Finite Element Model of the Electrical Machine Rotor

The FE model of the rotor is created in ABAQUS[TM], cf. (Clappier and Gaul, 2016). Figure 4(a) shows the FE model which consists of the laminated stack, rotor shaft, inner bearing rings and two balancing discs. The geometry is slightly simplified to reduce the number of finite elements. The mesh is created as a complete conform FE mesh using mainly linear brick elements with incompatible modes and a few linear wedge elements.
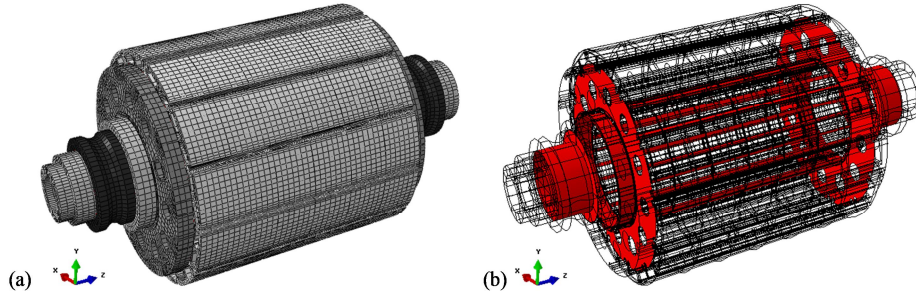
Figure 4. FE rotor model. (a) Mesh, (b) mechanical interfaces modelled by thin-layer elements (Clappier and Gaul, 2016)

Figure 4(b) depicts all mechanical interfaces. At these interfaces, so-called thin-layer elements are inserted to incorporate the joint stiffness and damping, cf. (Bograd et al., 2008) and (Gaul and Schmidt, 2014). Here, the TLEs are represented by linear brick elements with a small thickness to length ratio which can be as low as 1:1000, see (Bograd et al., 2008) and (Gaul and Schmidt, 2014). The dynamical behavior of each mechanical interface is described by one thin layer (TL) using a linearized orthotropic material model (cf. Section 3.2) (Bograd et al., 2008). All TLEs in one thin layer get the same stiffness and damping properties which can be identified experimentally on a generic lap joint (Gaul et al., 2011). In general, joint properties are load-dependent, cf. (Clappier et al., 2015b), (Gaul et al., 2016) and (Gaul et al., 2015). However, for applications with homogeneous contact pressure distributions at the interfaces, a homogenized parametrization of the TLEs can be efficiently applied (Bograd et al., 2008), (Clappier et al., 2015b). Otherwise, a load-dependent parametrization of the TLEs is necessary, see (Clappier et al., 2015b) and (Gaul et al., 2016). Figure 5 shows that the application requirement of a homogeneous contact pressure is fulfilled for the considered rotor. Due to the homogeneous contact pressure on the laminated stack in the set-up of Section 2.2 (Clappier and Gaul, 2015), the rotor application is well-suited for further investigations.
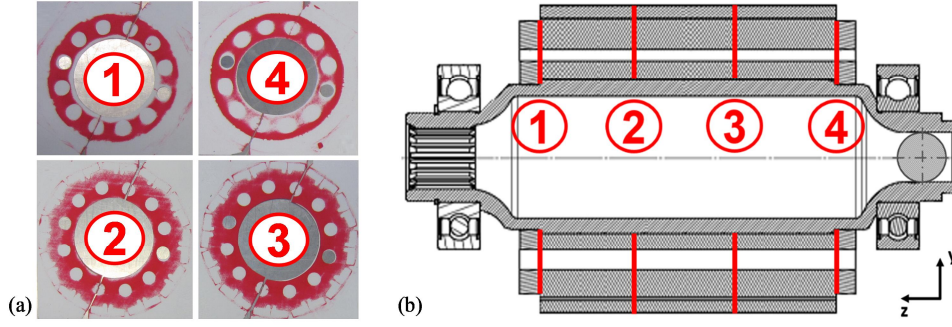
Figure 5. (a) Contact pressure measured via Fujifilm Prescale films at (b) different rotor positions (Clappier and Gaul, 2016)

3.2 Numerical Modal Analysis without Rotor Spin Speed

In order to prove the quality of the FE model, a numerical modal analysis (NMA) without boundary conditions and inner bearing rings is done. The equation of motion for free undamped vibrations

$$M \cdot \ddot{x} + K \cdot x = 0 \tag{4}$$

is transformed into the frequency domain by assuming time harmonic vibrations. This leads to the following eigenvalue problem (cf. Dassault Systèmes Simulia Corp. (2014))

$$\left(\alpha_k^2 \cdot M + K\right) \cdot \phi_k = 0 \ . \tag{5}$$

M is the mass matrix, K the real-valued stiffness matrix, x the displacement vector and $\ddot{x}$ the acceleration vector of the whole system. α_k and ϕ_k are the purely imaginary eigenvalue and real-valued eigenvector of mode k, respectively. Because the structural damping of mechanical joints, materials and laminated stacks can be considered to be frequency-independent in a wide frequency range ((Bograd et al., 2008), (Clappier and Gaul, 2015) and (Gaul et al., 2011)), the model of constant hysteretic damping can be efficiently applied to describe the damping of the system by a complex stiffness matrix K^* (cf. (Bograd et al., 2008), (Clappier et al., 2015a) and (Gaul and Schmidt, 2014))

$$K^* = K + j \cdot \left[\sum_{c=1}^{N_c} K_c \cdot \eta_c + \sum_{i=1}^{N_i} K_i \cdot \eta_i \right] \tag{6}$$

The first term of K^* represents the real-valued system stiffness matrix. The second and third terms are imaginary terms and represent the material and joint damping of all mechanical components (index c) and interfaces (index i). The last two terms are built-up by a summation over all products of the real-valued component or interface stiffness matrix (K_c, K_i) and its corresponding structural damping loss factor η_c or η_i. Values for η_c (excepted for the laminated rotor stack) and η_i are taken from (Gaul et al., 2011). Substituting K in equation (5) by K^* leads to a complex eigenvalue problem with complex eigenvalues and eigenvectors (Bograd et al., 2008). These are different from those of equation (5).

The joint stiffness of each interface is modeled by an orthotropic elasticity matrix D_i, cf. (Bograd et al., 2008) and (Gaul and Schmidt, 2014).

$$D_i = \begin{bmatrix} 0 & 0 & 0 & 0 & 0 & 0 \\ & 0 & 0 & 0 & 0 & 0 \\ & & D_{33} & 0 & 0 & 0 \\ & & & 0 & 0 & 0 \\ & sym. & & & D_{55} & 0 \\ & & & & & D_{66} \end{bmatrix} \tag{7}$$

The values of D_i are chosen according to Figure 6(a) such that the normal and tangential behavior of the joint is represented. The normal contact stiffness D_{33} is chosen to be 10…50% of the Young's modulus of the contacting materials, cf. (Netzmann, 2013). The shear moduli D_{55}, D_{66} are equal in their magnitudes and can be computed by equation (8) based on the contact area A and tangential stiffness k_T (both from the generic lap joint) and the TLE thickness h (Bograd et al., 2008). Thereby, the elasticity law for shear is used by assuming only small deformations $\gamma \ll 1$ (Figure 6(a), cf. (Bograd et al., 2008)). Data for k_T are taken from (Gaul et al., 2011).

$$D_{55} = D_{66} = \frac{k_T \cdot A}{h} \tag{8}$$

For physical reasons, all other diagonal terms of D_i should be zero. However, for numerical reasons values nearly zero are chosen (Bograd et al., 2008). Because of the interface geometries, it is necessary to use local Cartesian coordinates for one part of the TLEs and local cylindrical coordinates for the other part. In the case of using cylindrical coordinates, the diagonal terms of D_i have to be re-sorted.
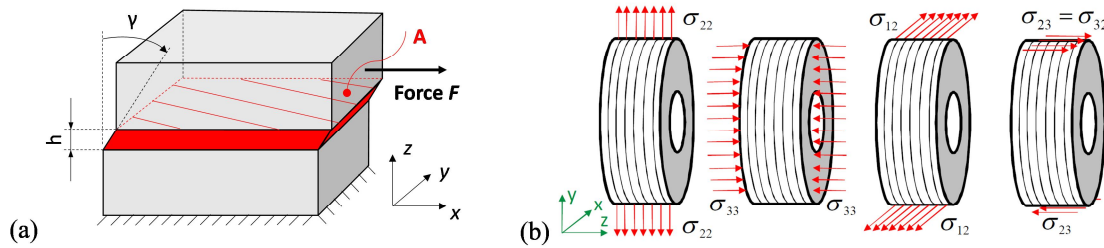
Figure 6. (a) Deformed thin-layer element (Bograd et al., 2008), (Clappier and Gaul, 2016), (b) illustration of laminated rotor stack properties (Clappier et al., 2015a)

The loss factor η_c, Young's modulus E_t in axial direction and shear modulus G_t of the laminated rotor stack can be obtained from measurement results of a dilatation and shear test which are carried out at a pre-stress condition corresponding to the rotor pre-stress condition. In order to define the component stiffness matrix K_c of the laminated stack, a transversely isotropic material model is used (Clappier et al., 2015a). The inverse of the elasticity matrix D_c is shown in equation (9), cf. (Clappier et al., 2015a) and (Dassault Systèmes Simulia Corp., 2014).

$$\varepsilon_c = D_c^{-1} \cdot \sigma_c$$

$$
\begin{bmatrix}
\varepsilon_{11} \\
\varepsilon_{22} \\
\varepsilon_{33} \\
2 \cdot \varepsilon_{12} \\
2 \cdot \varepsilon_{13} \\
2 \cdot \varepsilon_{23}
\end{bmatrix}
=
\begin{bmatrix}
1/E_p & -v_p/E_p & -v_{tp}/E_t & 0 & 0 & 0 \\
-v_p/E_p & 1/E_p & -v_{tp}/E_t & 0 & 0 & 0 \\
-v_{pt}/E_p & -v_{pt}/E_p & 1/E_t & 0 & 0 & 0 \\
0 & 0 & 0 & 1/G_p & 0 & 0 \\
0 & 0 & 0 & 0 & 1/G_t & 0 \\
0 & 0 & 0 & 0 & 0 & 1/G_t
\end{bmatrix}
\cdot
\begin{bmatrix}
\sigma_{11} \\
\sigma_{22} \\
\sigma_{33} \\
\sigma_{12} \\
\sigma_{13} \\
\sigma_{23}
\end{bmatrix}
\tag{9}
$$

ε_c, σ_c, E and G are the strain vector, stress vector, Young's modulus and shear modulus (Dassault Systèmes Simulia Corp., 2014), respectively. The indices t and p denote 'transverse' and 'in-plane' (Dassault Systèmes Simulia Corp., 2014). While E_t and G_t can be identified experimentally, all other quantities are given by the properties of a single electrical sheet, see (Clappier et al., 2015a). This becomes clearer by the illustrations in Figure 6(b). Further details are given in (Clappier et al., 2015a).

3.3 Rotor Dynamics Simulation

In this section, rotordynamic computations are done dependent on rotor spin speed. Thereby, further matrices in the equation of motion must be taken into account. Because of the asymmetric rotor geometry, rotordynamic analyses are carried out meaningfully in rotational coordinates fixed to the rotor, see (Friswell et al., 2012), (Genta, 2005) and (Vollan and Komzsik, 2012). Thus, the rotor stiffness matrix stays constant in time for a fixed rotor speed, cf. (Friswell et al., 2012). According to (Genta, 2005) and (Vollan and Komzsik, 2012), the equation of motion in the rotating coordinate system is given by

$$M \cdot \ddot{g} + \left(D + 2\Omega \cdot C \right) \cdot \dot{g} + \left(K - \Omega^2 \cdot Z + \Omega^2 \cdot K_G + \Omega \cdot K_D \right) \cdot g = F(t) \tag{10}$$

Thereby, M represents the general mass matrix, D the viscous damping matrix, C the gyroscopic matrix containing Coriolis effects, K the general stiffness matrix, Z the centrifugal matrix, K_D the geometric stiffness matrix, K_D the circulatory matrix, g the displacement vector, $\ddot{g}$ the acceleration vector and $F(t)$ the excitation force vector in rotating coordinates. In this work, the viscous damping matrix D (containing internal and external damping described by a viscous model) is not applied. Therefore, the matrix K_D also drops out. Internal damping is included by the complex stiffness matrix (see equation (6)). External damping is not considered because of the generally small damping of ball bearings (Gasch et al., 2006). For ball bearings, a (transversely) isotropic elastic bearing model is assumed for simplicity. In general, the bearing stiffness is different in vertical and horizontal direction, see (Gasch et al., 2006) and (Krämer, 1993). The radial bearing stiffness k_B is computed by equation (11) (Krämer, 1993) as a function of rotor spin speed dependent on the occurring unbalance forces (which act in the planes of both balancing discs), gravity force and speed-dependent external application forces. Thereby, z, d and F are the number of ball elements, ball diameter and bearing force. The bearing stiffness is included by connector elements in ABAQUS (Dassault Systèmes Simulia Corp., 2014) representing a "spring" stiffness which is incorporated into K during FE matrix assembling process. The bearing A is modeled to be axially rigid (using either a displacement boundary condition or a very high connector stiffness) and the bearing B without axial connector stiffness.

$$k_B = 1.3 \cdot z^{2/3} \cdot d^{1/3} \cdot F^{1/3} \qquad [N/\mu m] \tag{11}$$

3.4   Computation of Electromagnetic Forces

For the computation of electromagnetic airgap forces and torque at a certain operational point of the electrical machine, a 2D magnetic FE model is built up (cf. also (Arkkio et al., 2010), (Funieru and Binder, 2014) or (Pellerey et al., 2012)) using the software FEMAG (Reichert, 2011). Thereby, it is assumed that both, stator and rotor are of equal axial length and perfectly aligned to each other (in axial direction). In addition, it is assumed that no noteworthy axial forces occur in the airgap. Figure 7(a) depicts the created and used FE model which is a full model over 360° in order to examine the effects of dynamical rotor eccentricities. The considered PMSM has six pole pairs, 36 stator teeth and three phases.

In order to compute the magnetic force densities, a fine FE mesh is required in the airgap (cf. (Humbert et al., 2012) and (Reichert, 2011)) to attain sufficient computation accuracy. It is also recommended to use rectangular finite elements of equal size along the circumference for better accuracy, see (Cai et al., 2001), (Funieru and Binder, 2014) and (Reichert, 2011). In this work, first-order rectangular elements are used (Reichert, 2011) to mesh the airgap. Thereby, a mesh of equidistant increments of 0.25° is created along the circumference. For meshing rotor and stator first-order triangular elements are used. Rotor movement is modelled by the moving band technique, see (Funieru and Binder, 2014). Hereby, the airgap is remeshed for each rotor position after a rotational step (Funieru and Binder, 2014). For the computation of electromagnetic force densities in the airgap, different methods are discussed in literature, like Maxwell stress tensor, virtual work / co-energy method, Coulomb virtual work or Arkkio method, cf. (Cai et al., 2001), (Funieru and Binder, 2014), (Gieras and Wing, 2002), (Popescu, 2006) and (Wang et al., 2008). In this work, radial and tangential force densities are calculated using FEMAG based on Maxwell stress tensor (Reichert, 2011). This method is the most popular one and commonly used for excitation force computations in vibro-acoustic analyses of electrical machines, see (Funieru and Binder, 2014), (Gieras and Wing, 2002) and (Popescu, 2006).

During FE computation, the magnetic vector potential $\vec{A}$ is solved for all FE nodes as primary field variable, see (Gieras and Wing, 2002) and (Wang et al., 2008). Thereby, only the normal/radial flux density is satisfying continuity at the interface of different media/materials (e.g. interface air/iron) (Cai et al., 2001). Because of discontinuous tangential flux densities at the interface (see (Gieras and Wing, 2002) and (Popescu, 2006)), the global torque and local force densities are evaluated in this work on a circular path in the middle of the airgap, see Figure 7(b). This procedure is also recommended by other authors (Cai et al., 2001), (Funieru and Binder, 2014), FEMAG (Reichert, 2011) and (Wang et al., 2008). Furthermore, three FE layers of squared first-order rectangular FEs are used to mesh the airgap, cf. Figure 7(b) and (Cai et al., 2001), (Funieru and Binder, 2014), (Reichert, 2011), (Wang et al., 2008). The layer in the middle is used to apply the moving band technique (Funieru and Binder, 2014).
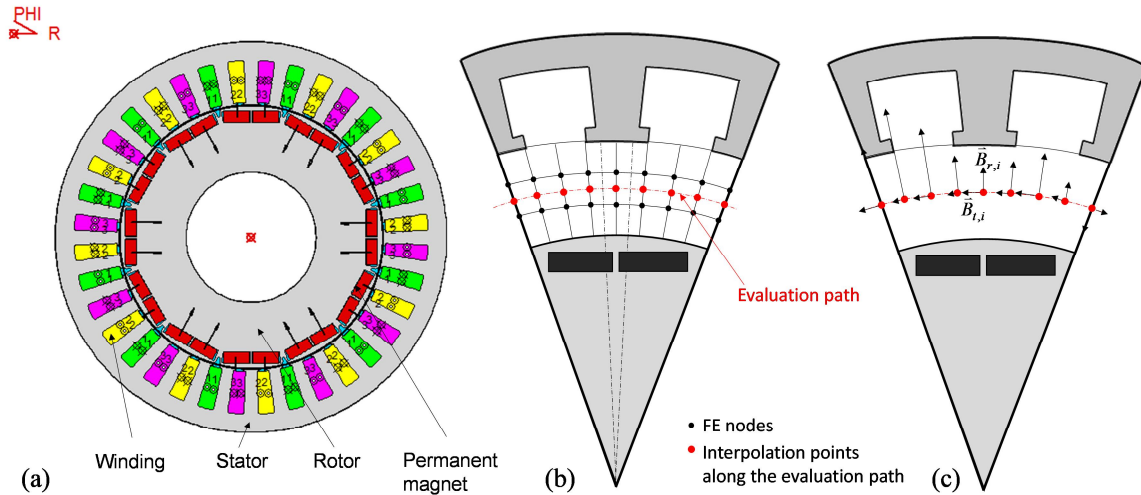
Figure 7. (a) 2D electromagnetic model (FE mesh not depicted because of the fine resolution), (b) evaluation path, (c) flux densities along evaluation path

Based on the magnetic vector potential $\vec{A}$ in the airgap (which only has one z-component in 2D, cf. Gieras and Wing (2002)), the magnetic flux density $\vec{B}$ is evaluated by

$$\vec{B} = rot(\vec{A}) \tag{12}$$

(Gieras and Wing, 2002) for all finite elements along the circular evaluation path. Due to the used linear elements, the 2D magnetic flux density vector has constant components within an element, see (Gieras and Wing, 2002) and (Popescu, 2006). From these values, the radial and tangential flux densities are interpolated at the interpolation points (feedback FEMAG support) on the evaluation path (cf. PLT1-file), Figure 7(c). Based on radial and tangential flux densities (B_r, B_t) at the interpolation nodes and magnetic permeability of air μ_0, the radial and tangential force densities (p_r, p_t) can be computed by the equations in (13) using Maxwell Stress Tensor, see (Cai et al., 2001), (Gieras and Wing, 2002) and (Humbert et al., 2012).

$$p_r = \frac{1}{2\mu_0} \cdot \left(B_r^2 - B_t^2 \right) \quad , \quad p_t = \frac{1}{\mu_0} \cdot B_r \cdot B_t \tag{13}$$

Physically, the computed force densities in the airgap middle represent stresses which cause attraction or repulsion forces between rotor and stator. In mechanics, stresses are internal quantities that describe the internal loading of a material and are therefore not visible without any body cuts. To deal with that issue and make the "internal" airgap forces "visible", a "magnetic-mechanical coupling element" is introduced, see Figure 8(a,b).
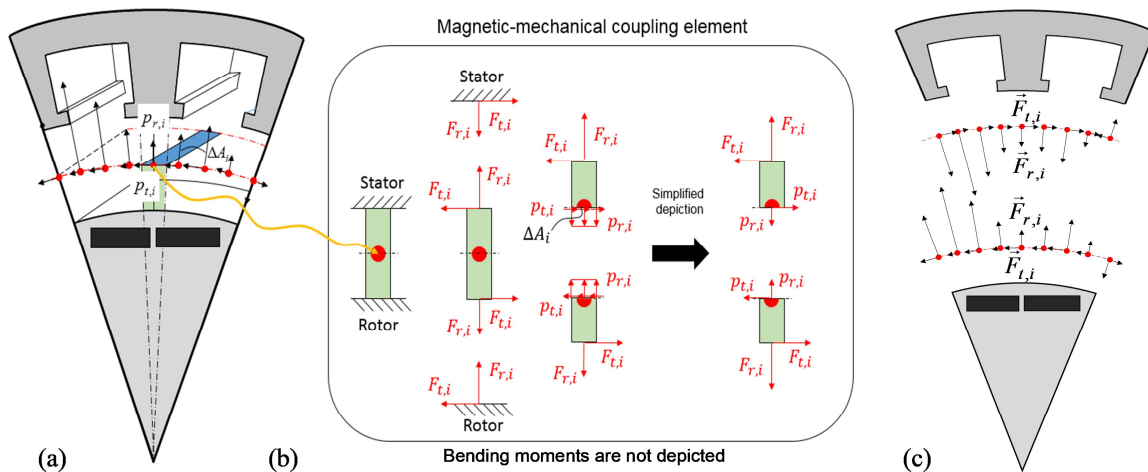
Figure 8. (a) Force density distribution, (b) magnetic-mechanical coupling element and (c) stator and rotor orientated "internal" airgap forces

333

This coupling element represents a mechanical stress element between the rotor and stator surfaces and includes the computed electromagnetic force density as internal load, see Figure 8(b). Thus, this model enables to interpret physically actio-reactio forces in the airgap (between rotor and stator) by means of internal forces which can be computed along the evaluation path (Figure 8(c)) through multiplication of force densities with the corresponding action area, Figure 8(a,c). The sum of rotor and stator oriented internal airgap forces Figure 8(c) have to be zero.

In order to carry out vibro-acoustic computations, the "internal" rotor and stator forces have to be transformed from the airgap middle onto the rotor and stator surfaces where they physically act. Thus, the internal forces become active forces on the mechanical structure. The applied transformation process is presented exemplarily for "internal" forces acting at one interpolation point i on the evaluation path, see Figure 9(a). Firstly, rotor oriented radial forces are moved along their action line onto the rotor surface. Secondly, the tangential forces are moved parallel to their force action line onto the rotor surface. In order to yield the same force conditions after parallel translation of tangential forces, an additional moment has to be added, see Figure 9(b). The superscript "LS" denotes the location in the airgap middle while "Sz" and "Ra" characterize forces on stator teeth and rotor surface.
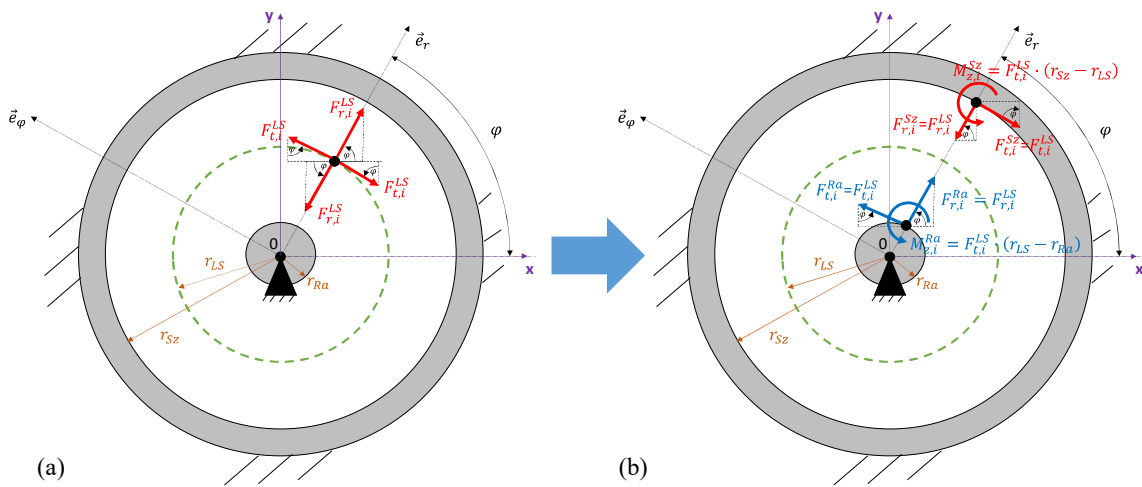
Figure 9. Transformation of internal "airgap forces" (a) into rotor and stator surface forces (b)

This procedure is done on both sides, for the rotor and stator. However, the focus of this paper is given to rotor dynamics and the corresponding excitation forces. Therefore, the process describing the transformation of surface forces into nodal forces for the structural FE model is only explained for the rotor side. At any rate, the same procedure can also be applied on stator side. However, the force transformation step into the rotating coordinate system is not required to examine stator or housing vibrations.

For reasons of computational accuracy and efficiency, the electromagnetic FE mesh is usually designed much finer (due to the considered small airgap) as the vibro-acoustic FE model, cf. (Humbert et al., 2012). To carry out rotor dynamic computations, the transformed rotor surface forces (Figure 10(a)) have to be summarized in a suited way at the nodes of the mechanical rotor FE model. Firstly, all moments $M_{z,i}^{Ra}$ in Figure 10(a) are replaced by equivalent tangential force pairs which are summarized with the already given tangential loads in Figure 10(a). Secondly, all radial and modified tangential rotor surface forces are transformed into the rotating coordinate system (Figure 10(b)) which is used for rotor dynamics computation. Lastly, all rotor surface forces within equidistant angular distances are summarized as resultant components at the surface FE nodes of the rotor model taking equivalent force pairs into account (Figure 10(c)).
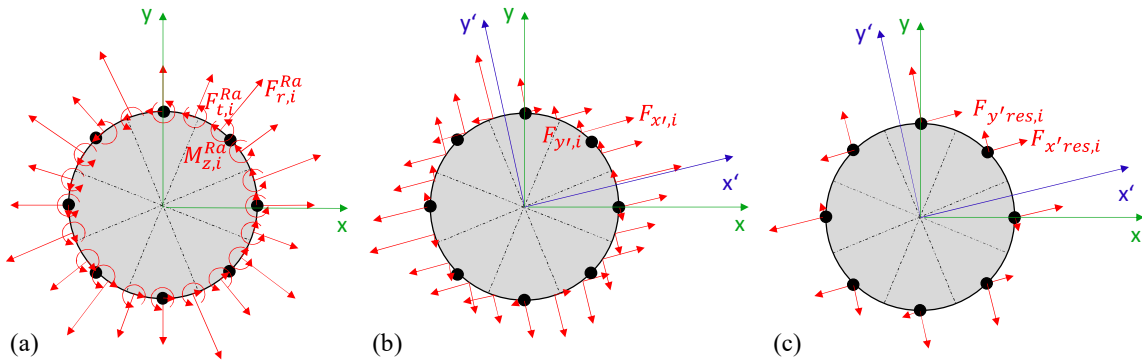
Figure 10. Rotor surface loads in (a) stationary coordinates (x,y), (b) in rotating coordinates (x',y')
and (c) summarized rotor forces acting on FE nodes of the structural model

The FE mesh of the rotor is extruded in the region of the laminated stack. Thus, the transformed resultant nodal forces (see Figure 10(c)) can be equally distributed along FE nodes in axial direction for mapping on a 3D structural FE mesh. In other words, the resultant force at one angular position (Figure 10(c)) is divided by the number of corresponding axial nodes at this position. Thus, all nodal forces are equal in magnitude and direction at one angular position (cf. (Pellerey et al., 2012) and (Shiohata et al., 2011)). The advantage of the proposed force transformation algorithm is the conservation of resulting torque as well as radial and tangential forces (originally obtained in the middle of the air gap), even after the transformation what is in contrast to available projection methods, like given in (Dupont et al., 2014).

4   Computational Results

4.1   Numerical Modal Analysis without considering Rotor Spin Speed

Table 1 shows the results of a NMA and EMA for two equivalent built-up rotors. A good agreement for the first five eigenfrequencies and mode shapes can be obtained. The experimental grid is fine enough to resolve all considered modes reliably. The modal damping of the first two modes is also predicted quite well but the prediction error increases at higher frequencies. However, the 'general' trend (except mode 3) is predicted correctly.

Table 1. Comparison of numerical and experimental rotor eigenfrequencies, mode shapes and damping
(Clappier and Gaul, 2016)

4.2   Rotordynamic Vibration Response due to Electromagnetic Force Excitation

In general, magnetic forces consist of many time and spatial harmonics (Gieras et al., 2006). Figure 11 shows for example the vibration response (in rotating coordinates) due to electromagnetic force excitation (on the laminated stack) for the 36th time harmonic order ($k=36$) without and with dynamical rotor eccentricity ε_d. The

magnetic forces of the 36th time harmonic order are obtained by a one-dimensional fast fourier transformation (FFT) of the nodal rotor surface forces. Without rotor eccentricity, the radial forces acting on the rotor cancel itself and only a torsional excitation occurs (Figure 11(a)). With eccentricity, a resultant radial force, the so-called unbalanced magnetic pull (UMP) (Friswell et al., 2012), occurs in addition to the torsional excitation leading to a superimposed radial rotor deflection. Thus, the rotordynamic response has to be determined within acoustical computations of electrical machines because the vibrations are transmitted to connected systems and the motor housing where undesirable sound can be caused.

(a)   (b)
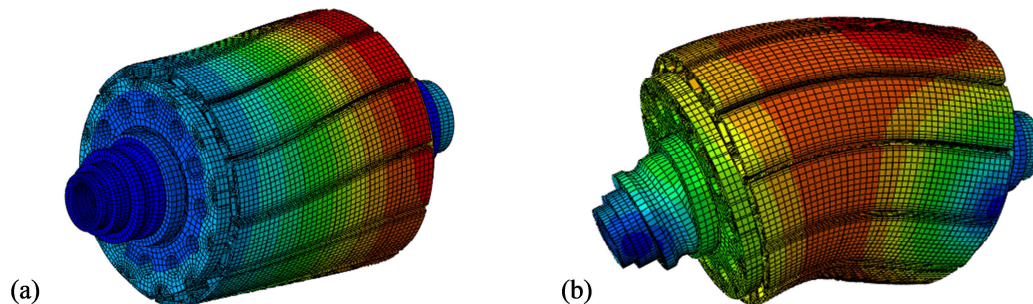
Figure 11. Rotor vibration response due to electromagnetic forces for time harmonic order $k = 36$ in rotating coordinates for dynamical rotor eccentricity (a) $\varepsilon_d = 0$ mm and (b) $\varepsilon_d = 0.25$ mm (Clappier and Gaul, 2016)

5   Conclusions and Outlook

Stator housing and rotordynamic vibrations must be taken both into account if acoustical computations of electrical machines are carried out. Especially rotor vibrations can be transmitted to connected systems of the powertrain and affect its overall acoustical behavior. Therefore, a finite element model of the rotor is presented in order to predict rotordynamic responses. The material properties of the laminated rotor stack are determined experimentally and incorporated by a transversely isotropic material model. Mechanical joints are modeled by thin-layer elements and damping by the model of constant hysteretic damping. A numerical modal analysis leads to a good agreement with the experiment. Furthermore, rotordynamic responses due to electromagnetic force excitation with and without dynamical rotor eccentricity are examined. Thereby, a new method is presented to transform the magnetic forces from a 2D electromagnetic onto a 3D mechanical finite element mesh.

References

Arkkio, A.; Nepal, B.R.; Sinervo, A.: Electromechanical interaction in a synchronous reluctance machine. In: *Proc. of SPEEDAM 2010*, IEEE, Pisa, Italy, June 14-16, (2010), 501-506.

Bograd, S.; Schmidt, A.; Gaul, L.: Joint Damping Prediction by Thin Layer Elements. In: *Proc. of IMAC XXVI: A Conference and Exposition on Structural Dynamics*, Orlando, USA, February 4–7, (2008).

Cai, W.; Pillay, P.; Reichert, K.: Accurate computation of electromagnetic forces in switched reluctance motors. In: *Proc. of 5-th ICEMS 2001*, IEEE, Shenyang, China, August 18-20, (2001), 1065-1071.

Clappier, M.; Gaul, L.: Experimental Investigation of Structural Damping of Laminated Stacks of Electrical Machine Rotors. In: P. Pennacchi, ed., *Mechanisms and Machine Science*, Vol. 21, *Proceedings of the 9th IFToMM International Conference on Rotor Dynamics*, Springer, (2015), 613-624.

Clappier, M.; Gaul, L.; Westkämper, E.: Experimental Determination of Material Properties in Stacking Direction of Laminated Stacks belonging to Electrical Machine Rotors using a Dilatation Test. In: *Proc. of the 22nd International Congress on Sound and Vibration*, Florence, Italy, July 12-16, (2015a).

Clappier, M.; Ehrlich C; Gaul, L.: Linearized Joint Damping Model for Assembled Structures with Inhomogeneous Contact Pressure using Thin-Layer Elements. In: *Proc. of the 22nd International Congress on Sound and Vibration*, Florence, Italy, July 12-16, (2015b).

Clappier, M.; Gaul, L.: Frequency Domain Dynamic Simulation of an Electrical Machine Rotor. In: *Proc. of the 23rd International Congress on Sound and Vibration*, Athens, Greece, July 10-14, (2016).

Crandall, S.H.; Kurzweil, L.G.; Nigam, A.K.: On the Measurement of Poisson's Ratio for Modeling Clay. *Journal of Experimental Mechanics*, 11(9), (1971), 402-407.

Dassault Systèmes Simulia Corp.: *Abaqus Documentation, Abaqus Analysis User's Guide and Abaqus Theory Guide*. Release 6.14, Providence, RI, USA, (2014).

Desai, C. S.; Zaman, M. M.; Lightner, J. G.; Siriwardane, H. J.: Thin-layer element for interfaces and joints, *International Journal for Numerical and Analytical Methods in Geomechanics*, 8, (1984), 19-43.

Dupont, J. B.; Aydoun, R.; Bouvet, P.: Simulation of the noise radiated by an automotive electric motor: influence of the motor defects. *SAE Int. J. Alt. Power*, 3(2), (2014), 310-320.

Friswell, M.; Penny, J.E.T.; Garvey, S.D.; Lees A.W.: *Dynamics of Rotating Machines*. Cambridge University Press, New York, (2010, reprinted 2012).

Funieru, B.; Binder, A.: 3D numerical calculation method of electrical machines with time efficient air gap coupling and stabilized torque and force calculation. In: *Proc. ICEM2014*, Berlin, Sept. 3-5, (2014), 954-960.

Gasch, R.; Nordmann, R.; Pfützner, H.: *Rotordynamik*. 2. Auflage, Springer, Berlin, (2006).

Gaul, L.; Lenz, J.: Nonlinear dynamics of structures assembled with bolted joints. *Acta Mechanica*, 125, (1997), 169-181.

Gaul, L.; Clappier, M.; Einbock, S.: Frequency Domain Structural Dynamic Simulation of an Electrical Machine Housing. In: *Proc. of the 23rd Int. Congress on Sound and Vibration*, Athens, July 10-14, (2016).

Gaul, L.; Schmidt, A.; Bograd, S.: *Modellierung von Werkstoff- und Fügestellendämpfung in der FEM*. FVV-Vorhaben 984, Heft 940, (2011).

Gaul, L.; Hanss, M.; Schmidt, A.; Ehrlich, C.: *Modellierung von Werkstoff- und Fügestellendämpfung in der FEM unter Berücksichtigung von Unsicherheiten*. FVV-Vorhaben 1119, Heft R572, (2015).

Gaul, L.; Schmidt, A.: Experimental Identification and Simulation of Rotor Damping. In: *Proc. of IMAC XXXII: A Conference & Exposition on Structural Dynamics*, Orlando, USA, February 3-6, (2014).

Genta, G.: *Dynamics of Rotating Systems*. Springer, New York, (2005).

Gieras, J.F.; Wang, C.; Lai, J.C.: *Noise of Polyphase Electric Motors*. CRC Press, Boca Raton, (2006).

Gieras, J.F.; Wing, M.: *Permanent Magnet Motor Technology*. Dekker, New York, (2002).

Humbert, L.; Pellerey, P.; Cristaudo, S.: Electromagnetic and structural coupled simulation to investigate NVH behavior of an electrical automotive powertrain. *SAE Int. J. Alt. Power*, 1(2), (2012), 395-404.

Krämer, E.: *Dynamics of Rotors and Foundations*. Springer, Berlin, (1993).

McCloskey, A.; Arrasate, X.; Almandoz, G.; Hernandez, X.; Salgado, O.: Vibro-acoustic finite element analysis of a permanent magnet synchronous machine. In: *Proc. of 9th EURODYN*. Porto, Portugal, (2014), 3321-3328.

Netzmann, H.D.: *NVH-Akustik-Berechnung am Motorrad-Motor unter Berücksichtigung unsicherer Modelparameter*. PhD thesis, University of Stuttgart, Der Andere Verlag, Uelvesbüll, (2013).

Pellerey, P.; Lanfranchi, V.; Friedrich, G.: Numerical simulations of rotor dynamic eccentricity effects on synchronous machine vibrations for full run up. In: *Proc. of ICEM2012*, Marseille, September 2-5, (2012), 3008-3014.

Popescu, M.: Prediction of the electromagnetic torque in synchronous machines through Maxwell stress harmonic filter (HFT) method. *Journal Electrical Engineering*, 89(2), (2006), 117-125.

Reichert, K.: *FEMAG Benutzer-Anleitung*. ETH Zürich, Zürich, (2011).

Shiohata, K.; Kusama, R.; Ohtsu, S.; Iwatsubo, T.: The study on electromagnetic force induced vibration and noise from a normal and an eccentric universal motors. In: *Proc. of PIERS*, Marrakesh, Morocco, March 20-23, (2011), 1654-1660.

Siegl, G.: Das Biegeschwingungsverhalten von Rotoren, die mit Blechpaketen besetzt sind. PhD thesis, TU Berlin, Berlin, (1981).

Vollan, A.; Komzsik, L.: *Computational Techniques of Rotor Dynamics with the Finite Element Method*. CRC Press, Boca Raton, (2012).

Wang, L.; Cheung, R.W.; Ma, Z.; Ruan, J.; Peng, Y.: Finite-element analysis of unbalanced magnetic pull in a large hydro-generator under practical operations. *IEEE Trans. on Mag.*, 44(6), (2008), 1558-1561.

Graduate School of Excellence advanced Manufacturing Engineering in Stuttgart (GSaME), University of Stuttgart, 70569, Stuttgart, Germany
marcel.clappier@gsame.uni-stuttgart.de

Institute for Nonlinear Mechanics (INM), Research Group Prof. Gaul, University of Stuttgart, 70569, Stuttgart, Germany
lothar.gaul@inm.uni-stuttgart.de